Atlas-based method for model updating in image-guided liver surgery

Logan W. Clements[a], Prashanth Dumpuri[a], William C. Chapman[b], Robert L. Galloway[a,c,d], and Michael I. Miga[a]

[a]Vanderbilt University, Dept. of Biomedical Engineering, Nashville, TN
[b]Washington University School of Medicine, Dept. of Surgery and Cell Biology, St. Louis, MO
[c]Vanderbilt University, Dept. of Surgery, Nashville, TN
[d]Vanderbilt University, Dept. of Neurological Surgery, Nashville, TN

ABSTRACT

Similar to the well documented brain shift experienced during neurosurgical procedures, intra-operative soft tissue deformation in open hepatic resections is the primary source of error in current image-guided liver surgery (IGLS) systems. The use of bio-mechanical models has shown promise in providing the link between the deformed, intra-operative patient anatomy and the pre-operative image data. More specifically, the current protocol for deformation compensation in IGLS involves the determination of displacements via registration of intra-operatively acquired sparse data and subsequent use of the displacements to drive solution of a linear elastic model via the finite element method (FEM). However, direct solution of the model during the surgical procedure has several logistical limitations including computational time and the ability to accurately prescribe boundary conditions and material properties. Recently, approaches utilizing an atlas of pre-operatively computed model solutions based on *a priori* information concerning the surgical loading conditions have been proposed as a more realistic avenue for intra-operative deformation compensation. Similar to previous work, we propose the use of a simple linear inverse model to match the intra-operatively acquired data to the pre-operatively computed atlas. Additionally, an iterative approach is implemented whereby point correspondence is updated during the matching process, being that the correspondence between intra-operative data and the pre-operatively computed atlas is not explicitly known in liver applications. Preliminary validation experiments of the proposed algorithm were performed using both simulation and phantom data. The proposed method provided comparable results in the phantom experiments with those obtained using the traditional incremental FEM approach.

Keywords: image-guided surgery, liver surgery, soft tissue deformation, finite element method, laser range scanning

1. INTRODUCTION

Similar to the well documented brain shift experienced during neurosurgical procedures, intra-operative soft tissue deformation in open hepatic resections is the primary source of error in current image-guided liver surgery (IGLS) systems. Numerous avenues have been suggested to aid in the compensation for the experienced soft tissue deformation, including the use of intra-operative tomography and ultrasound. However, intra-operative computed tomography (iCT) and magnetic resonance (iMR) imaging equipment is extremely expensive and cumbersome in the operating room environment. Additionally, intra-operative ultrasound (iUS) provides low signal-to-noise, sparse images of the patient's anatomy. Ultimately, the goal for image-guidance is to update the high contrast, high resolution pre-operative tomograms to match the intra-operative presentation.
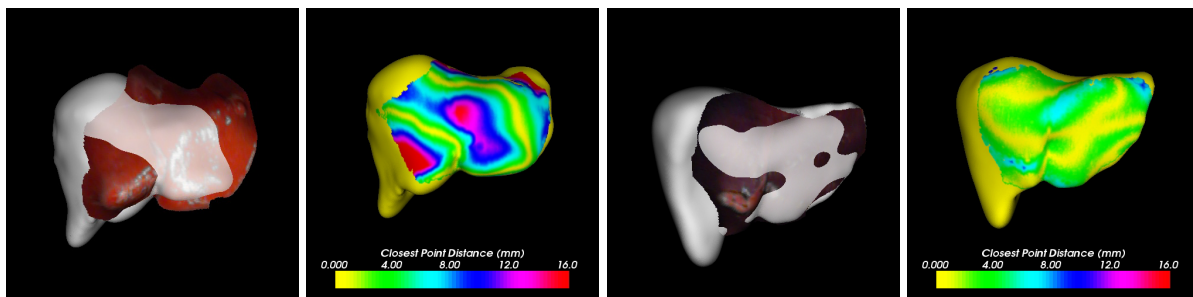
Correspondence:
Logan W. Clements
Department of Biomedical Engineering
Vanderbilt University
P.O. Box 351631, Station B
Nashville, TN 37235
logan.clements@vanderbilt.edu

Mathematical models, which have been used to model various mediators of the deformation in neurological surgery, have been proposed to provide the link between the pre-operative and intra-operative presentations. While direct solution of mathematical models, utilizing intra-operatively acquired displacements, during surgery seems to be of promise in facilitating deformation compensation, more recent work in atlas-based methods seem to provide a more realistic alternative. By simulating the range of deformation sources in a pre-operatively computed atlas and matching the intra-operative data to the atlas, compensation for soft tissue deformation can be performed with minimal user interaction and in a fraction of the time needed to directly solve the model.

While useful guidance information is provided by the rigid, surface-based registrations used in current IGLS procedures, it is quite clear that this information can be compromised by intra-operative soft tissue deformation. The significance of soft tissue deformation in the form of "brain shift" has been widely documented in neurosurgical procedures[1–7] and has been observed in our initial clinical experience in the performance of IGLS.[8] Figure 1 illustrates the range of soft tissue deformation imposed during clinical cased by the liver mobilization and packing procedures performed prior to resection.

Figure 1. Figures showing the results of ICP registration and the corresponding closest point distances for two clinical cases. The two sets of data demonstrate the inter-patient variability in the observed soft tissue deformation in open IGLS. Notice that the while the case presented in the left panels show significant portions of the surface with closest point distances in upwards of 2 cm, whereas a vast majority of the surface shown in right panels displays closest point distances of approximately 5 mm.

Based on the observed incidence of soft tissue deformation in IGLS, we seek to provide compensation via an atlas-based approach similar to that originally proposed by Davatzikos *et al.*[9] Atlas-based approaches to deformation compensation have shown great promise in neurosurgery applications[10, 11] and we seek to expand on this work such that it will be amenable to IGLS. It should be noted that the implementation of atlas-based deformation compensation techniques to IGLS presents a unique challenge based on the fact that exact correspondence between the intra-operatively acquired LRS data and the pre-operative liver surface is not known. In neurosurgical applications, this point correspondence can be determined and allows for the computation of intra-operative brain shift.[12]

1.1. Related Work

The use of LRS data to drive a bio-mechanical model of the liver was initially proposed by Miga *et al.*[13] Building on this work, Cash *et al.* proposed an incremental approach to solving the model.[14] Additionally, this work demonstrated the use of a deformation identifying rigid registration (DIRR) which provided a more meaningful alignment than a traditional ICP registration. Other groups, such as Brock *et al.*, have used time dependent models to describe the liver motion due to respiration.[15]

Recently, the use of atlas-based methods have been proposed for incorporation into IGS systems for the compensation of deformation. Dumpuri *et al.* have proposed the computation of a deformation atlas, provided by FEM solutions of a bio-mechanical model under a variety of conditions determined by *a priori* knowledge of the surgical procedure.[10, 11] The individual surface displacements predicted by the deformation atlas are then matched with those determined via cortical surface tracking with LRS using a constrained linear inverse model. Similar methods have been proposed by Davatzikos *et al.*[9] wherein a statistical approach based on principal component analysis (PCA), inspired by the work of Cootes *et al.*,[16, 17] is used to fit deformed data to the atlas.

1.2. Objective

The objective of this work is to develop an atlas-based model updating method that is amenable to the application of IGLS. As mentioned previously, the development of such a method represents novel work due to the lack of point correspondence information as opposed to brain applications. Preliminary validation of the proposed method will be provided in the form of simulation and phantom experiments. Additionally, a comparison between the phantom experiment results obtained with the proposed atlas-based approach and traditional incremental FEM implementation will be presented.

2. METHODS

2.1. Model Equations and Boundary Condition Implementation

We begin with the assumption that the liver is an isotropic solid with a linear stress-strain relationship as in the work of Cash *et al.*[14] The equation for a linear-elastic 3D solid at static equilibrium is:

$$\nabla \cdot \tilde{\sigma} = \mathbf{B} \tag{1}$$

where $\tilde{\sigma}$ represents the stress tensor and $\mathbf{B}$ represents the body forces acting on the object. Hooke's law relates mechanical stress tensor ($\tilde{\sigma}$) to the mechanical strain tensor ($\tilde{\varepsilon}$) via the following relationship:

$$\tilde{\sigma} = C\tilde{\varepsilon} \tag{2}$$

where C represents the material stiffness matrix, which is dependent on the Young's Modulus (E) and Poisson's ratio (ν) material properties. By making the appropriate substitutions for C, a system of partial differential equations (PDEs) can be expressed in terms of the displacement vector ($\mathbf{u}$):

$$\frac{E}{2(1+\nu)}\nabla^2\mathbf{u} + \frac{E}{2(1+\nu)(1-2\nu)}\nabla(\nabla \cdot \mathbf{u}) = \mathbf{B} \tag{3}$$

In order to solve the system equations in Equation 3 over the liver mesh domain, the Galerkin weighted residual method is applied using linear basis functions. Using this technique, the system of PDEs reflecting the displacement vectors ($\mathbf{u}$) at each node in the tetrahedral mesh can be compiled in matrix form using the following relation:

$$K\mathbf{u} = \mathbf{B} \tag{4}$$

The driving force behind generating deformations with an FEM model is provided by the prescription of the appropriate conditions along the boundary of the tetrahedral mesh. Similar to the conditions described by Cash *et al.*,[14] a set of three general boundary condition types will be used in the creation of the liver deformation atlas. The first type of condition we use is a Dirichlet zero displacement condition that is used to signify fixed regions of the liver that do not experience any displacement. This condition is generally prescribed to regions on the posterior surface of the right lobe. The second type is condition used is a Dirichlet condition of specified non-zero displacement. We use this condition to model the liver packing performed prior to resection, typically prescribed to regions beneath the left lobe. The final type of condition used in the liver model is a Neumann "stress free" condition used to signify regions that are unrestricted by force.

In the application of displacement boundary conditions for anatomical soft tissue (i.e. the aforementioned Dirichlet conditions), it is often desirable to express the movement of the boundary in a coordinate system that is relative to the shape of the organ of interest. A number of studies have shown that the specification of displacement boundary conditions normal to the surface can be quite helpful in providing tissue-mimicking deformations.[13, 14, 18] In certain scenarios it may be useful to allow an organ surface to slide along a supporting plane tangent to the surface and not deform in the normal direction. Additionally, it may also be useful to apply deformation in a direction normal to the surface and also allow the tissue to slide tangent to the displacing

surface (e.g. the depression of a tissue surface with a retractor). These types of conditions require stress-free conditions to be imposed tangent to (i.e. $\vec{t_1}$ and $\vec{t_2}$) the specified normal displacement direction ($\vec{n}$):

$$\sigma_{t1} = \sigma_{t2} = 0, u_n = u_s \tag{5}$$

where $\sigma_{t1,t2}$ are the stresses applied tangent to the organ surface and u_s signifies the specified displacement normal the surface. These so called "mixed" boundary condition are implemented via the normal-tangential procedure described by Engelman $et\ al.$[19]

2.2. Deformation Atlas Creation

A primary factor in determining the success of atlas-based methods of registration is the process of atlas creation to ensure that the range of possible deformations, based on the pre-operative plan for a particular patient and $a\ priori$ knowledge of surgical loading conditions, are contained within the atlas. The process of atlas construction begins with the generation of a volumetric mesh of the liver which is derived from the surface description provided by a segmentation of the pre-operatively obtained tomographic image volumes. We employ the algorithm described by Sullivan $et\ al.$[20] to generate the tetrahedral liver mesh. Once the mesh has been created, a set of boundary conditions, range of patient orientations (i.e. gravity directions), and range of material properties are selected based on $a\ priori$ information about the surgical procedure. Once the set of conditions have been determined, the model is run for each permutation of the sets of conditions and the deformed volumetric and surface meshes for each model solution are then saved for incorporation into the surface matching algorithm.

2.3. Iterative Closest Atlas Algorithm

Once the set of model solutions have been computed and the deformed liver volume meshes and surfaces have been compiled, the collected intra-operative data (i.e. LRS scan of the liver surface) is then fit to the atlas via the Iterative Closest Atlas (ICAt) Algorithm. Similar to the work performed by Dumpuri $et\ al.$,[10, 11] fitting the intra-operative data to the pre-operatively computed model atlas is performed via the following linear relationship:

$$\mathbf{A}\omega = \mathbf{d} \tag{6}$$

where $\mathbf{A}$ is an $[(N \times 3) \times M]$ model atlas matrix, ω is an $[M \times 1]$ vector representing weighting coefficients for each model solution, $\mathbf{d}$ is an $[(N \times 3) \times 1]$ vector representing the intra-operative data, M represents the number of model solutions contained in the atlas, and N is the total number of surface nodes of the tetrahedral mesh that have corresponding points within the intra-operative data set $\mathbf{d}$. Note that the expression in Equation 6 inherently implies a known correspondence between mesh surface points and the intra-operative surface data points. Being that this correspondence is not known with any certainty, an iterative approach is used whereby point correspondence is updated at each iteration following computation of the current atlas solution based on the values of the weighting coefficients (ω) at the current iteration. Given an initialization of the weighting parameters (ω_0) and assuming a rough initial alignment of the intra-operative data ($\mathbf{d}$) to the pre-operative image surface, the algorithm proceeds as follows:

Step 1. Let iteration number $i = 0$. Given the $a\ priori$ distribution of the weighting parameters (ω_0), compute the current model solution using the relationship $A = \mathbf{A}\omega_0$.

Step 2. Compute the rigid body transformation (T_{d-A}) between the data point set ($\mathbf{d}$) and A using the closest point operator to determine point correspondence.

Step 3. Transform the data point set ($\mathbf{d}$) using transformation computed in **Step 2**: $\mathbf{d} = T_{d-A}(\mathbf{d})$.

Step 4. Compute the closest points on A to the transformed data points $\mathbf{d}$, which we will call A_{cp}. Build a new atlas matrix ($\mathbf{A}_{cp}$) containing only the indices of the points in A_{cp}.

Step 5. Compute the closest points on $\mathbf{d}$ to the point set A_{cp}, which we will call d_{cp}.

Step 6. Compute the new set of weighting parameters (ω_i) by solving the linear equation $\mathbf{A}_{cp}\omega_i = d_{cp}$.

Step 7. Increment iteration count ($i = i + 1$). Compute new model solution using the relationship $A = \mathbf{A}\omega_i$. Repeat **Step 2** through **Step 7** until i exceeds maximum number or residual error tolerance is met.

We choose a least squares formulation to obtain the solution of Equation 6 in **Step 6** of the above description of the ICAt algorithm, which is equivalent to the following matrix equation:

$$\omega = (\mathbf{A}^T\mathbf{A})^{-1}\mathbf{A}^T\mathbf{d} \tag{7}$$

Due to the fact that the condition number of the matrix $\mathbf{A}^T\mathbf{A}$ is extremely large, the inverse formulation is 7 is ill-conditioned in the sense of Hadamard.[21] In order to stabilize the results of the solution of Equation 7, we employ a Tikhonov regularization process where we seek to find an ω to minimize:

$$\|\mathbf{A}\omega - \mathbf{d}\|^2 + \beta^2\|\omega\|^2 \tag{8}$$

where $\|\cdot\|$ is the Euclidean norm and β is called the Tikhonov factor. The least squares formulation in Equation 7 now becomes:

$$\omega = (\mathbf{A}^T\mathbf{A} + \beta^2 I)^{-1}\mathbf{A}^T\mathbf{d} \tag{9}$$

where I is the $M \times M$ identity matrix. We chose to use the following Tikhonov factor (β^2) used by Jaochimowicz *et al.*[22] for the solution of a similar inverse problem:

$$\beta^2 = \lambda\Big[1/N\sum_{i=1}^{N}\mathbf{A}^T\mathbf{A}(i,i)\Big][d_{err}]^2 \tag{10}$$

where the parameter λ is a weighting parameter that represents the magnitude of β^2, which is empirically determined based on the convergence of the problem. The middle term represents the trace of the matrix $\mathbf{A}^T\mathbf{A}$, which improves the conditioning of the matrix by reducing the gap between its higher and lower eigenvalue. The final term ($[d_{err}]^2$) is a relative mean square error term used to decrease the weight of β^2 as the method converges and is defined as follows:

$$d_{err} = \sqrt{\frac{\sum_{i=1}^{N}|\Delta d_k(i)|^2}{\sum_{i=1}^{N}|d_{cp}(i)|^2}} \tag{11}$$

where $\Delta d_k = A_{cp} - d_{cp}$ at iteration k and i is the point index. In other words, d_{err} represents the relative error between the true point location (d_{cp}) and the atlas reconstructed point location (A_{cp}) at each iteration. The difference in $\Delta d_k = A_{cp} - d_{cp}$ between iterations is used as one of the stopping criteria.

2.4. Validation

2.4.1. Simulation Experiment

The initial validation experiments for the ICAt algorithm involved the performance of a simulation experiment. First, an atlas was created using one of the liver meshes obtained from the segmentation of a clinical data set (shown in Figure 2). The following parameters were used in the generation of the atlas: initial gravity vector ($\vec{g}$) = (0.7071,0.7071,0.0), Young's modulus (E) = 15 kPa, Poisson's ratio (ν) = 0.47 and ρ = 1000.0 kg/m^3. The distribution of boundary conditions used to generated the atlas are shown in Figure 2. The patient orientation was varied to create a atlas of 121 solutions by rotation of $\vec{g}$ about the y- and z-axes where the values of the rotation angles (θ^y and θ^z) were varied between -50° and 50° in increments of 10°. In order to generate a set of source data, simulating deformed LRS scans, five separate deformed meshes were created by using randomly

generated rotation angles for θ^y and θ^z within the range of that used to create the atlas (i.e. $\theta^y, \theta^z \in [-50°, 50°]$). Once the deformed meshes were created, a subset of the surface points, which were obtained by extracting the region corresponding with the coverage of the acquired LRS data (shown in Figure 2), were used to realistically simulate the surface coverage of true intra-operative data. It should be noted that the parameters used to create the deformation atlas were chosen such that considerable deformations would be imposed and not to reflect parameters that would be used in the generation of a deformation atlas to model actual intra-operative data.
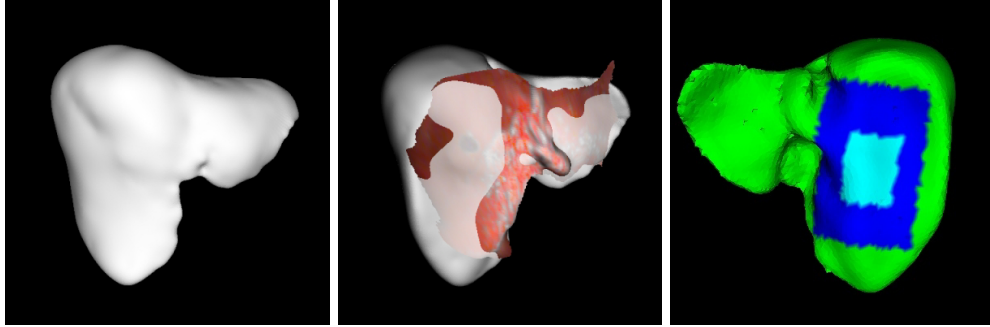

Figure 2. The liver surface mesh (left), the ICP registration result (center), and the boundary condition distribution (right) used to create the deformation atlas for the ICAt simulation experiments. The ICP registration result is shown to give the reader an indication of the size of the simulated scans relative to the full liver surface. For the distribution of boundary conditions, the green area corresponds with the Neumann "stress free" condition, the light blue area corresponds with the Dirichlet "fixed" condition, and the dark blue region corresponds with the normal-tangential Dirichlet "fixed" condition where $u_n = 0$).

Once the deformation atlas and the sets of simulated LRS data had been generated, the ICAt algorithm was used to fit the simulated LRS data to the atlas. The maximum number of iterations was set to 50 and the convergence tolerance was set to 1e-5 mm. The weighting factor (λ) for the Tikhonov regularization parameter in Equation 10 was set to 0.1. Additionally, no further changes were made to the initial pose of the simulated LRS surfaces. Unlike the data used in the phantom and clinical examples, point correspondence is known exactly in the simulation data. Therefore, the least-squares problem in Equation 9 was solved directly to provide a "gold standard" comparison for the ICAt results. For the direct LSQ solution the regularization parameter (β^2) was set directly to 0.1.

2.4.2. Phantom Experiments

A set of experiments were performed using the poly (dimethyl) siloxane (rubber silicone) model of the liver which was used in the phantom studies performed by Cash *et al.*[14, 23] The silicon phantom is rigidly attached to a plexiglass base and is surrounded by a set of seven white Teflon spheres resting atop cylindrical holders of various heights. These spheres can be localized in both CT and LRS images reliably and serve to provide reliable landmarks for point-based registrations between the various imaging data collected. Additionally, a set of six styrofoam spheres (radii approximately 1-1.15 cm) are embedded within the silicon phantom which represent mock tumors. These styrofoam spheres are easily distinguishable from the surrounding silicone in CT images and the centroids are obtained using a region growing algorithm provided by the Analyze software package (Mayo Clinic, Rochester, MN). The locations of the centroids of the six mock tumors serve as subsurface targets to quantify performance of the algorithm and to facilitate a comparison between the proposed atlas-based method and the traditional incremental FEM approach. The positions of the mock tumors within the liver phantom are shown in Figure 3.

In order to simulate the deformations imposed by the packing and mobilization procedure performed during liver resections, a plastic object (approximate height of 3.8 cm) was placed in two locations beneath the phantom. A large nylon screw placed through the middle portion of the right lobe of the silicon liver served to hold other regions stationary. The two selected locations were the left lobe region and the middle of the inferior ridge beneath Couinaud segments III, IV, and V. For the first deformation the mock tumors 1 and 2 experienced the
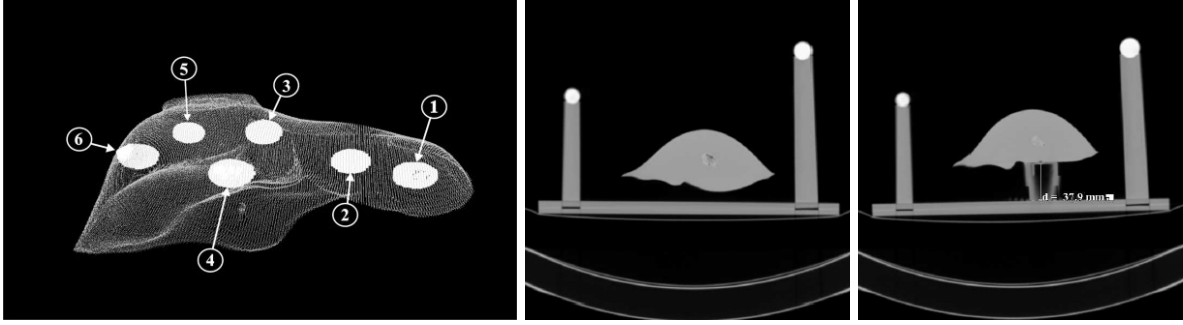
Figure 3. The segmented CT surface (left) of the phantom with sub-surface tumors and corresponding CT slices for non-deformed (middle) and deformed (right) phantom configurations. A plastic object (approximate height of 38 mm) was placed underneath the left lobe of the liver phantom to simulate deformation imposed by liver packing performed during surgery.

most shift and tumors 4 and 6 experienced the most shift for the second displacement. Corresponding slices from one of the deformed image volumes (deformation 1) and the non-deformed CT image volumes are shown in Figure 3.

To perform the ICAt algorithm on the phantom data sets, two atlases were created based on *a priori* knowledge of the two imposed deformations. The imposed deformations were modeled as normal displacement conditions in the regions of the boundary that corresponded with the areas under which the plastic object was placed. The imposed normal displacement (u_n) was varied from 2 cm to 6 cm in increments of 1 cm. In addition to varying the normal displacement lengths, a set of three region sizes of the imposed normal displacement condition was also used. Finally, the material property of Young's modulus was varied between 25 kPa and 40 kPa in increments of 5 kPa. The variation of normal displacement region, displacement length, and Young's modulus led to an atlas size of 60 solutions for each deformation. Once the atlases were created, initialization for the ICAt algorithm was determined by performing ICP registrations between the deformed LRS scan data for each deformation and non-deformed surface of the phantom. Convergence of the algorithm was determined if the difference in the surface residuals between successive iterations was less than 1e-5 mm or if the surface residual error remained stable and no longer decreased after several iterations. The scaling factor (λ) in the Tikhonov regularization parameter defined in Equation 10 was chosen to be 0.1 for both deformation cases. The output displacements determined from the ICAt algorithm were then used to warp the un-deformed CT images volumes and the new positions of the tumor centroids were determined. The errors between these centroid locations and the true tumor centroids as determined by the ICAt registrations were then compared with analogous results to those received by the incremental FEM implementation proposed by Cash *et al.*[14]

3. RESULTS

3.1. Simulation Experiments

A summary of the simulation results is shown in Table 1 and Table 2. In these tables, three separate error measurements are reported. The scan error measurement describes the true error between the scan region points was determined by the known point correspondence. The mesh error measurement describes the true error over all of the nodes within the mesh using the known point correspondence. Finally, the scan residual error metric (only reported for the ICAt data) describes the RMS closest point distance between the simulated surface date and the closest points on the mesh. In order to give a reference for the initial deformations, Table 1 shows the measurement of the scan and mesh errors prior to the performance of any registration or deformation compensation. The data reported in Table 2 shows the results of both the ICAt algorithm and the direct LSQ method of solution. The data presented shows that for four of the five trials, the ICAt algorithm does not converge to the true solution and yield significantly larger errors than the "gold standard" fit to the deformation atlas.

Trial	Before Solution	
	Scan Error	Mesh Error
1	15.95(50.80)	11.78(63.28)
2	18.98(48.99)	14.13(59.24)
3	16.74(59.93)	9.14 (72.23)
4	20.45(52.62)	13.33(57.94)
5	16.52(56.96)	10.28(69.06)
mean	**17.73(53.86)**	**11.73(64.35)**

Table 1. Summary of the scan error (mm) and mesh error (mm) values before the performance of any compensation methods for the five sets of trial data in the ICAt simulation study. The values shown in parentheses are the maximum errors.

Trial	ICAt			Direct LSQ	
	Scan Residual	Scan Error	Mesh Error	Scan Error	Mesh Error
1	1.16(3.99)	3.33(5.38)	2.57(5.41)	0.19(0.32)	0.25(0.48)
2	1.84(6.53)	6.45(8.79)	5.47(9.87)	0.10(0.18)	0.12(0.21)
3	1.58(4.70)	4.30(5.93)	4.35(6.71)	0.16(0.60)	0.13(0.75)
4	1.67(5.08)	4.10(6.51)	4.92(11.69)	0.11(0.24)	0.12(0.29)
5	0.12(0.38)	0.12(0.38)	0.24(0.53)	0.20(0.63)	0.21(0.77)
mean	**1.27(4.14)**	**3.66(5.40)**	**3.51(6.84)**	**0.15(0.39)**	**0.17(0.50)**

Table 2. Summary of the results of the ICAt simulation study which compares the surface error (mm) and mesh error (mm) values obtained from the ICAt solution and surface error (mm) and mesh error (mm) values obtained from a direct LSQ solution using the known point correspondence over the five trials. Additionally, the closest point surface residual (mm) for the ICAt algorithm at convergence is included. The values in parentheses represent the maximum error values (mm).

3.2. Phantom Experiments

Qualitative results and a summary of the mock tumor target errors for the left lobe deformation (deformation 1) trial are shown in Figure 4 and Table 3, respectively. As shown by the graphical results in Figure 4, the residual error between the deformed LRS surface and the deformed CT surface via ICAt solution displacements is drastically improved over both the PBR and ICP alignments. Additionally, the summary of the tumor error measurements shown in Table 3 shows that the ICAt solution provided considerable improvement over the initial ICP alignment errors and is comparable with the results shown for the incremental FEM initialized with the DIRR.

The qualitative results and a summary of the mock tumor target errors for the inferior ridge deformation (deformation 2) trial are shown in Figure 5 and Table 3, respectively. As shown by the graphical results in Figure 5, significant improvement in the surface matching was obtained by the ICAt solution in comparison to the PBR alignment between the surfaces. However, the qualitative results do not show significant improvement over the ICP alignment between the deformed LRS data and the pre-deformation phantom surface. The mock tumor target error data shown in Table 3 shows that the results of the ICAt algorithm provided target error comparable to those received by the incremental FEM implementation.

4. DISCUSSION

The preliminary validation results from the simulation and phantom experiments show promise in the proposed ICAt algorithm for providing a viable compensation strategy for intra-operative soft tissue deformation. Specifically, the results obtained by the phantom experiments shown in Figure 4, Figure 5, and Table 3 indicate that the proposed atlas-based approach provided comparable results to those achieved by the incremental FEM approach developed by Cash *et al.*[14] These results seem to provide further impetus for work on improving this
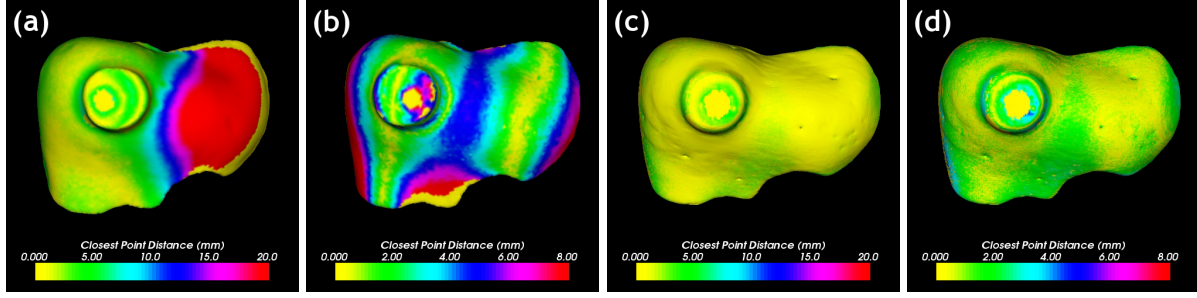
Figure 4. Qualitative ICAt results for phantom deformation 1 (left lobe deformation). The closest point distances between deformed LRS data and non-deformed CT surface after point based registration based on sphere fiducials (a), ICP registration (b), and closest point distances between deformed LRS surface and deformed CT surface based on ICAt solution (c,d). For reference, the mean residuals for the PBR, ICP, and ICAt registrations were found to be 16.83 mm (43.44 mm max), 3.65 mm (19.43 mm max), and 1.20 mm (11.11 mm max), respectively.
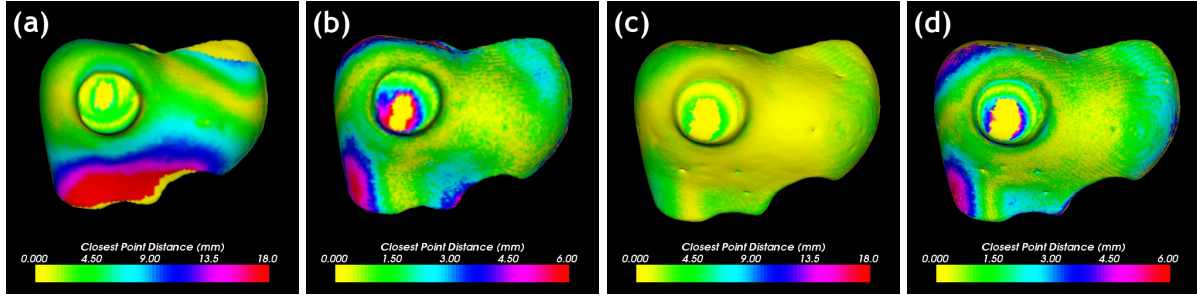
Figure 5. Qualitative ICAt results for phantom deformation 2 (inferior ridge deformation). The closest point distances between deformed LRS data and non-deformed CT surface after point based registration based on sphere fiducials (a), ICP registration (b), and closest point distances between deformed LRS surface and deformed CT surface based on ICAt solution (c,d). For reference, the mean residuals for the PBR, ICP, and ICAt registrations were found to be 7.23 mm (28.89 mm max), 1.73 mm (22.31 mm max), and 1.65 mm (20.83 mm max), respectively.

Tumor	Deformation 1				Deformation 2			
	ICP	ICP ICAt	DIRR Model	ICP Model	ICP	ICP ICAt	DIRR Model	ICP Model
1	7.0	4.6	5.6	2.8	3.5	3.2	2.9	3.1
2	6.8	3.6	4.2	2.3	2.0	1.8	1.1	1.2
3	8.4	3.8	3.1	5.5	1.9	1.8	1.2	1.4
4	8.1	2.4	5.3	3.5	5.3	3.6	3.8	5.3
5	5.4	5.3	0.4	4.9	4.1	3.8	1.4	4.5
6	8.0	3.7	4.2	6.9	6.1	3.4	4.0	5.5
mean	**7.3**	**3.9**	**3.8**	**4.3**	**3.8**	**2.9**	**2.4**	**3.5**

Table 3. Comparison of tumor target error (mm) phantom experiment results obtained by the ICAt algorithm (initialized with ICP registration) and the incremental FEM (initialized with ICP and DIRR) for deformation 1 (left lobe deformation) and deformation 2 (inferior ridge deformation). For reference, the tumor error (mm) is shown after the performance of an ICP registration (used to initialize the ICAt and incremental FEM).

method since the intra-operative solution times and user interaction are minimized relative to the incremental FEM method.

While the ICAt solution provided considerable improvement over the initial ICP alignment errors and is comparable with the results shown for the incremental FEM initialized with the DIRR for deformation 1 (shown in Figure 4), the improvement in surface and sub-surface target alignment is less significant for the simulated inferior ridge deformation show in Figure 5. A potential explanation for the relatively poorer performance of the ICAt algorithm on the phantom data for deformation 2 is that the pre-computed atlas does not contain the appropriate information to describe the true imposed deformation. While the results are not as accurate as in the first deformation case, the relative speed improvement over the incremental approach and comparability of the results in terms of tumor target error values is comforting.

Additionally, the results presented from the phantom study are quite intriguing since the ICAt solution converged to the true solution for only one of the five trials. One possibility is that the sampling of deformations within the atlas is too far (i.e. the size of the angular increments is too large). However, if the problem was inherent to the created deformation atlas, one would expect to see similar errors in the direct LSQ fit. A more realistic explanation for the behavior of the ICAt algorithm would be convergence to a local minimum. Being that the size of the deformations is quite large, the initial positioning for such large deformation could possibly be quite poor and lead to a local minimum convergence of the algorithm. Additionally, it is quite interesting that the values of the scan and mesh errors for trial 5 are different between the ICAt solution and the direct LSQ solution even though, presumably, both reflect the same solution. This could be due to a numerical artifact resulting from the difference in the regularization parameter used in the two methods. Based on the results from the simulation studies, there may be a need to incorporate a weighting scheme (similar to that used in weighted ICP methods presented by several groups[24, 25]) to bias point correspondence in order to increase the robustness of the algorithm.

Ultimately, the viability of utilizing an atlas-based approach to model updating is reliant on the ability to pre-operatively compute complete atlases that contain the full array of the deformations imposed by the various surgical loads. Incomplete atlases will limit the utility of the proposed ICAt algorithm in terms of yielding pertinent information to guide surgical procedures. Additionally, the presented method uses a very simple linear objective function without any constraining terms. Other work, such as that presented by Dumpuri *et al.*,[11] have demonstrated the effectiveness of incorporating shape constraints within the linear model to improve accuracy. When making the transition from phantom and simulation to clinical data, it will certainly be necessary to incorporate such constraints into the algorithm.

5. CONCLUSION

The preliminary data provided in validation of the proposed atlas-based approach to model updating in IGLS indicate that the method should provide a more realistic and viable method to compensate for soft tissue deformation during surgical procedures. The ability to use *a priori* information to pre-compute model solutions with allows for faster solution times and circumvents the need to prescribe boundary conditions within the OR is very exciting. By increasing our knowledge of the soft tissue deformation imposed by the surgical procedure in open hepatic resections we hope to be able to create more complete deformation atlases and ultimately provide model-updated images for guiding these procedures. Future work will entail the incorporation of the biasing of point correspondence within the registration method to increase the robustness of the algorithm, improving the linear LSQ objective function to constrain the solutio method and validation with regards to clinical data sets.

ACKNOWLEDGMENTS

REFERENCES

1. P. Kelly, B. Kall, S. Goerss, and F. Earnest, "Computer-assisted stereotaxic laser resection of intra-axial brain neoplasms," *J. Neurosurg.* **64**, pp. 427–439, Mar 1986.

2. H. Nauta, "Error assessment during 'image guided' and 'imaging interactive' stereotactic surgery," *Comput. Med. Imaging Graph.* **18**, pp. 279–287, Jul 1994.

3. D. Roberts, A. Hartov, F. Kennedy, M. Miga, and K. Paulsen, "Intraoperative brain shift and deformation: a quantitative analysis of cortical displacement in 28 cases," *Neurosurgery* **43**, pp. 749–758, Oct 1998.

4. D. Hill, C. Maurer, R. Maciunas, J. Barwise, J. Fitzpatrick, and M. Wang, "Measurement of intraoperative brain surface deformation under a craniotomy," *Neurosurgery* **43**(3), pp. 514–526, 1998.

5. C. R. Maurer, D. L. G. Hill, A. J. Martin, H. Y. Liu, M. McCue, D. Rueckert, D. Lloret, W. A. Hall, R. E. Maxwell, D. J. Hawkes, and C. L. Truwit, "Investigation of intraoperative brain deformation using a 1.5-T interventional mr system: Preliminary results," *IEEE Trans. Med. Imaging* **17**(5), pp. 817–825, 1998.

6. A. Nabavi, P. M. Black, D. T. Gering, C. F. Westin, V. Mehta, R. S. Pergolizzi, M. Ferrant, S. K. Warfield, N. Hata, R. B. Schwartz, W. M. Wells, R. Kikinis, and F. A. Jolesz, "Serial intraoperative magnetic resonance imaging of brain shift," *Neurosurgery* **48**(4), pp. 787–797, 2001.

7. C. Nimsky, O. Ganslandt, S. Cerny, P. Hastreiter, G. Greiner, and R. Fahlbusch, "Quantification of, visualization of, and compensation for brain shift using intraoperative magnetic resonance imaging," *Neurosurgery* **47**, pp. 1070–1079, Nov 2000.

8. D. M. Cash, S. C. Glasgow, L. W. Clements, M. I. Miga, B. Dawant, Z. Cao, R. L. Galloway, and W. C. Chapman, "Concepts and preliminary data towards the realization of an image-guided liver surgery system," *Annals of Surgery* **In press**, 2006.

9. C. Davatzikos, D. Shen, A. Mohamed, and S. Kyriacou, "A framework for predictive modeling of anatomical deformations," *IEEE Trans. Med. Imaging* **20**, pp. 836–843, Aug. 2001.

10. P. Dumpuri and M. I. Miga, "Model-updated image guidance: A statistical approach to gravity-induced brain shift," in *Lecture Notes in Computer Science*, **2878**, pp. 375–382, Medical Image Computing and Computer-Assisted Intervention, Springer-Verlag, 2003.

11. P. Dumpuri, R. C. Thompson, B. M. Dawant, A. Cao, and M. I. Miga, "An atlas-based method to compensate for brain shift: Preliminary results," *Medical Image Analysis* **Accepted**, 2006.

12. T. Sinha, B. Dawant, V. Duay, D. Cash, R. Weil, R. Thompson, K. Weaver, and M. Miga, "A method to track cortical surface deformations using a laser range scanner," *IEEE Trans. Med. Imaging* **24**, pp. 767–781, June 2005.

13. M. Miga, D. Cash, Z. Cao, G. R.L., B. Dawant, and W. Chapman, "Intraoperative registration of the liver for image-guided surgery using laser range scanning and deformable models," *SPIE Medical Imaging 2003* **5029**, 2003.

14. D. Cash, M. Miga, T. Sinha, R. Galloway, and W. Chapman, "Compensating for intraoperative soft-tissue deformations using incomplete surface data and finite elements," *IEEE Trans. Med. Imaging* **24**, pp. 1479–1491, Nov. 2005.

15. K. M. Brock, J. M. Balter, L. A. Dawson, M. L. Kessler, and C. R. Meyer, "Automated generation of a four-dimensional model of the liver using warping and mutual information," *Medical Physics* **30**, pp. 1128–1133, Jun 2003.

16. T. F. Cootes and C. J. Taylor, "Combining point distribution models with shape models based on finite-element analysis," *Image and Vision Computing* **13**, pp. 403–409, June 1995.

17. T. F. Cootes, C. J. Taylor, D. H. Cooper, and J. Graham, "Active shape models - their traning and application," *Computer Vision and Image Understanding* **61**, pp. 38–59, Jan 1995.

18. M. Miga, K. Paulsen, J. Lemery, S. Eisner, A. Hartov, F. Kennedy, and D. Roberts, "Model-updated image guidance: initial clinical experiences with gravity- induced brain deformation," *IEEE Trans. Med. Imaging* **18**, pp. 866–874, Oct 1999.

19. M. S. Engelman and R. Sani, "The implementation of normal and/or tangential boundary conditions in finite element codes for incompressible fluid flow," *International Journal for Numerical Methods in Fluids* **2**, pp. 225–238, 1982.

20. J. Sullivan, G. Charron, and K. Paulsen, "A three-dimensional mesh generator for arbitrary multiple material domains," *Finite Elements in Analysis and Design* **25**(3-4), pp. 219–241, 1997.

21. A. N. Tikhonov and V. Y. Arsenin, *Solutions of Ill-Posed Problems*, V.H. Winston & Sons, 1977.

22. N. Joachimowicz, C. Pichot, and J. Hugonin, "Inverse scattering: an iterative numerical method for electromagnetic imaging," *IEEE Transactions on Antennas and Propagation* **39**, pp. 1742–1753, Dec. 1991.

23. D. M. Cash, T. K. Sinha, W. C. Chapman, H. Terawaki, B. M. Dawant, R. L. Galloway, and M. I. Miga, "Incorporation of a laser range scanner into image-guided liver surgery: Surface acquisition, registration, and tracking," *Medical Physics* **30**, pp. 1671–1682, Jun 2003.

24. L. Clements, D. Cash, W. Chapman, R. Galloway Jr., and M. Miga, "Robust surface registration using salient anatomical features in image-guided liver surgery," in *SPIE 2006 Medical Imaging, San Diego*, 2006.

25. C. R. Maurer, G. B. Aboutanos, B. M. Dawant, R. J. Maciunas, and J. M. Fitzpatrick, "Registration of 3-D images using weighted geometrical features," *Ieee Transactions on Medical Imaging* **15**(6), pp. 836–849, 1996.